Z-99 RAY-BASED STOCHASTIC INVERSION

ARIE VERDEL[1], DENNIS VAN DER BURG[2] and KEES WAPENAAR[2]
[1]Shell Exploration and Production Technology, Kessler Park 1, PO Box 60, 2280 AB Rijswijk-ZH, The Netherlands
[2]Delft Univ of Technology, Subfaculty of Applied Earth Sciences, Mijnbouwstr 120, 2628 RX Delft, The Netherlands

Summary

A new seismic inversion method, Ray-Based Stochastic Inversion (RBSI) is presented, which is founded on the high-frequency Asymptotic Ray Theory (ART) description of seismic waves and firmly links Kirchhoff-Helmholtz pre-stack depth migration (PreSDM) with Stochastic Inversion (SI) for reservoir properties. Results from synthetic data tests show that: (1) RBSI, contrary to SI, can correctly determine lateral layer-density variations, a requirement for preserved-amplitude PreSDM, and (2) RBSI can delineate the correct reservoir properties in cases where SI produces erroneous results because of dip-dependent migration stretch.

Ray-Based Stochastic Inversion Principle

For RBSI, the subsurface space $X \subset \mathbb{R}^3$ with surface boundary ∂X is parameterised as an over-burden macro-model overlying a layered target reservoir sequence (Fig. 1) and is thereby assumed to satisfy the standard ray-theoretical validity conditions [1] (elements $\vec{x}$ of X can be written as (x_1, x_2, x_3) with $x_3 > 0$ and ∂X as $x_3 = 0$). Instead of the 1D convolutional model of SI, in RBSI 3D elastic ray-tracing is used. In principle, any wave type and acquisition configuration can be handled by RBSI. In this paper, we limit ourselves to surface-recorded single P-reflections. The key vehicle for RBSI is then formed by a single pair of P-rays leaving a reflection point $\vec{x}_R \in \Sigma_{\mathrm{refl}}$ within the reservoir sequence at angles $\pm\theta$ to the normal-vector $\hat{n}(\vec{x}_R)$ of the reflection surface Σ_{refl} in $\vec{x}_R$. Layer parameters on the lower side of Σ_{refl} are iteratively updated using a Metropolis algorithm [2] whereby the mismatch between the modeled $\vec{u}(\vec{x}_s, \vec{x}_r, \vec{x}_R; t)$ and real $\vec{s}(\vec{x}_s, \vec{x}_r, \vec{x}_R; t)$ reflection is minimised: $\vec{u}(\vec{x}_s, \vec{x}_r, \vec{x}_R; t)$ is uniquely defined by the single source-receiver pair $(\vec{x}_s, \vec{x}_r)$, by initial directions $(\pm\theta, \phi)$ (measured from $\hat{n}(\vec{x}_R)$) in the plane of propagation at angle ϕ with the azimuth), by the migration velocity model $v_p(\vec{x})$ and by the source wavelet $\mathcal{F}_0(t)$ (Fig. 2). Ray-theory requires at least C_2-smoothness of Σ_{refl}, which has to be determined from reflection event picks on the migrated image. Furthermore, either two-point ray-tracing or interpolations are generally required, to find those values of θ and ϕ that lead to ray-emergence locations $\vec{x}_s$ and $\vec{x}_r$.

Numerical Examples

The leading term (denoted by zeros in equation below) of the formal asymptotic ray series expansion solution of the general elastodynamic equation can be expressed as, see [1]:

$$\vec{u}(\vec{x}_s, \vec{x}_r, \vec{x}_R;\ t) = \mathrm{Re}\left[\vec{u}^{(0)}(\vec{x}_s, \vec{x}_r, \vec{x}_R)F_0(t - \tau(\vec{x}_s, \vec{x}_r, \vec{x}_R))\right] \tag{1}$$

with $\vec{u}$ the asymptotic displacement field vector measured at $\vec{x}_r$ due to a wave emitted at $\vec{x}_s$ and reflected at $\vec{x}_R$. The isotropic point source is represented by $S(\vec{x}_s, t) = \mathcal{F}_0(t)A_0(\vec{x}_s)\delta(\vec{x} - \vec{x}_s)$, with A_0 the source strength. In order to allow handling of phase shifts due to passage of rays through caustics ($\mathrm{Im}[\vec{u}^{(0)}]$ can become nonzero), the bandlimited source signal function (source

wavelet) $\mathcal{F}_0$ has to be extended to the analytical wavelet $F_0(t) = \mathcal{F}_0(t) + i\mathcal{G}_0(t)$ with $\mathcal{G}_0$ the Hilbert transform of $\mathcal{F}_0$ (if caustics are absent: $\mathcal{G}_0=0$). The phase function or eikonal τ is real-valued.

The synthetic data tests have been performed using the simple model presented in Fig. 3: a 2.5D isotropic-elastic subsurface with constant $v_p=2500$ m/s, $v_p/v_s=1.7$ (resulting in straight rays), and Gaussian reflectors and layer-density variations. The x_3-component of the single P-wave reflection response of the n-th contrast can be calculated analytically for this model (thereby neglecting the minor amplitude loss for rays passing through density gradients) using the ART-expression:

$$u_3^{(0)}(\vec{x}_s, \vec{x}_r, \vec{x}_R) = \frac{A_0(\vec{x}_s)C_0(\vec{x}_s, \vec{x}_r, \vec{x}_R)C_1(\vec{x}_s, \vec{x}_r, \vec{x}_R)T(\vec{x}_R, \theta_n^+)R^+(\vec{x}_R, \theta_n^+)}{(l(\vec{x}_s, \vec{x}_R) + l(\vec{x}_R, \vec{x}_r))} \qquad (2)$$

with $A_0 = 1 \ \forall \vec{x}_s$, l the ray path lengths, $T = \prod_{i=1}^{n-1} T_i^-(\theta_i^-)T_i^+(\theta_i^+)$, the product of transmission losses of the ray-pair (while crossing $n-1$ contrasts in the overlying overburden plus reservoir) and C_0 the free surface correction factor. With our choice of model- and acquisition parameters the zero-offset particle velocity data set $\dot{u}_3(\vec{x}_s = \vec{x}_r;\ t)$ is caustic-free and only contains normal-incidence ($\theta_n^+ \equiv 0$)-reflections. The expressions for reflector curvature correction factor C_1 and Zoeppritz reflection coefficient R^+ in (2) then simplify to (subscripts 1 and 2 refer to upper and lower side of reflector respectively and r_c^+ = reflector radius of curvature at $\vec{x}_R$, measured from above; see [1, pp. 82–84]):

$$R^+(\vec{x}_R, \theta_n^+ = 0) = \frac{\rho_2(\vec{x}_R) - \rho_1(\vec{x}_R)}{\rho_2(\vec{x}_R) + \rho_1(\vec{x}_R)} \qquad (3)$$

$$C_1(\vec{x}_s = \vec{x}_r, \vec{x}_R) = \sqrt{\frac{r_c^+(\vec{x}_R)}{r_c^+(\vec{x}_R) + l(\vec{x}_s = \vec{x}_r, \vec{x}_R)}} \qquad (4)$$

Fig. 4 shows every 20th trace of $\dot{u}_3$ for 601 source/receiver-positions at 10 m spacing using a zero-phase bandpass wavelet. These data served as input for the comparative SI- and RBSI-tests. Preserved amplitude PreSDM of $\dot{u}_3$ reads ("$\langle \ \rangle$" denotes that R^+ is bandlimited):

$$\langle\, R^+(\vec{x}, \theta_n^+ = 0)\, \rangle = -\frac{2}{\pi v_0 T(\vec{x}, \theta_n^+ = 0)}\int_{-\infty}^{\infty}\int_{-\infty}^{\infty}\frac{\partial}{\partial t}\dot{u}_3(\vec{x}_s = \vec{x}_r;\ t)|_{t=t_d}\mathrm{d}x_{1r}\mathrm{d}x_{2r} \qquad (5)$$

in which t_d represents the two-way time between $\vec{x}$ and $\vec{x}_s = \vec{x}_r$, and $v_0 = v_p$. In Fig. 5 the data is shown after preserved-amplitude PreSDM using a laterally constant density model. A reasonable assumption, as we only have density information at the well location. Fig. 6 shows the difference between Fig. 5 and the migrated result using the correct laterally variable density model as obtained from RBSI. The differences become larger deeper down in the model because of the accumulating effect of incorrect transmissions. This is expressed in Fig. 7 (bottom) which shows the reflection amplitude of the 6th interface using a laterally constant density model (lower solid line) and the exact density model (upper solid line), in comparison with the theoretical reflection coefficient (dashed line). In the top of the same figure, inversion results are shown for the density of the 6th layer: SI (lower curve) versus RBSI (almost identical to theoretical curve). Error bars denote standard deviations.

In order to systematically investigate the detrimental effect of migration-induced wavelet stretch on SI, models were designed varying three parameters: layer-thickness, reflection-amplitude difference and reflector-dip (see insets in Figs. 8-10). In the same figures stretch-dependent and stretch-free model results are shown (in varwig and wiggle display respectively). The barplots represent the inversion results for SI and for RBSI respectively. It can be concluded that RBSI determines the density of the middle layer much better than SI.
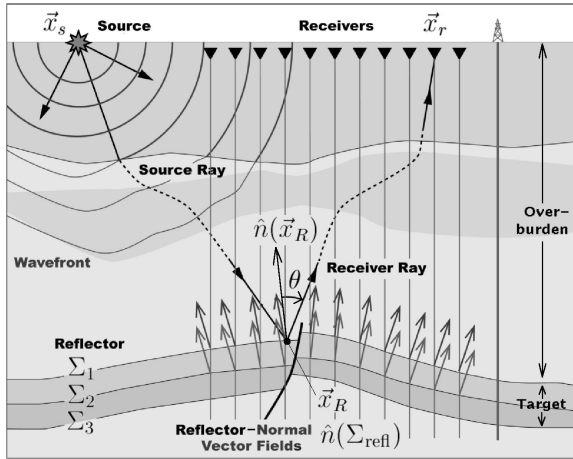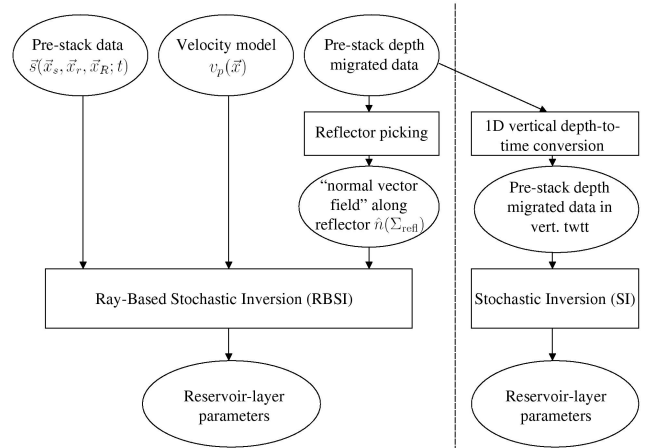
Figure 1: *Subsurface Parameterisation for RBSI.*

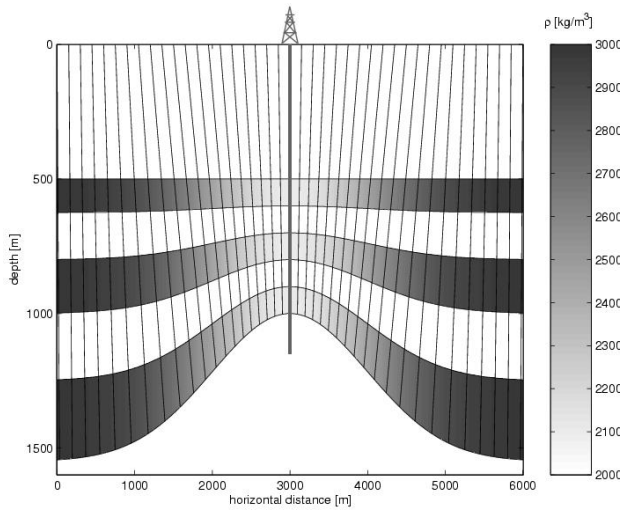Figure 2: *Flowsheet RBSI and SI for event-wise inversion of layer-parameters.*

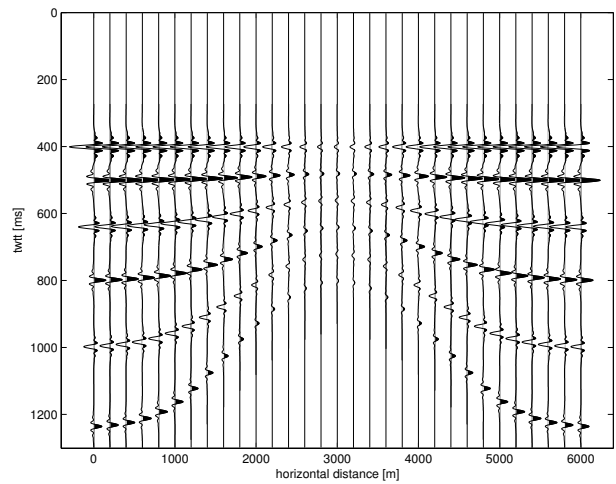Figure 3: *Zero-offset rays in Gaussian density model.*

Figure 4: *Dataset $\dot{u}_3$ corresponding to Fig. 3.*

Outlook

The results obtained so far indicate that investigation of more realistic models is opportune: RBSI's robustness should be tested in the presence of complex velocity models, velocity uncertainties, wavelet errors and noise in general. Also, extension to finite offset configurations will be investigated.

Acknowledgment

References

[1] V. Červený, I.A. Molotkov, and I. Pšenčík. *Ray Method in Seismology.* Univerzita Karlova, Praha, 1977.

[2] J. Leguijt. A promising approach to subsurface information integration. *EAGE Extended Abstracts*, pages L–35, June 2001.
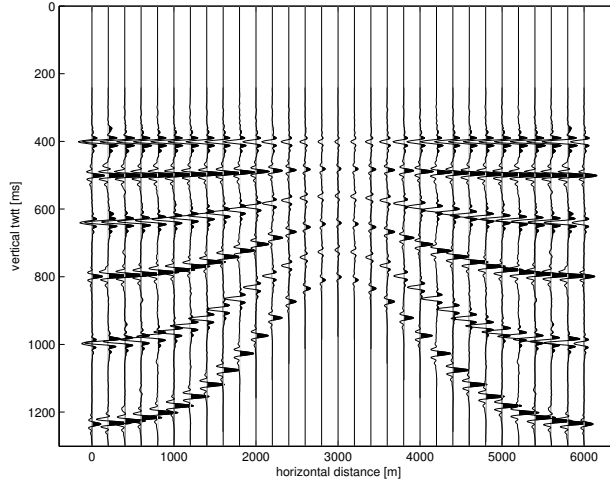
Figure 5: *Preserved-amplitude zero-offset depth migration with laterally constant density model.*
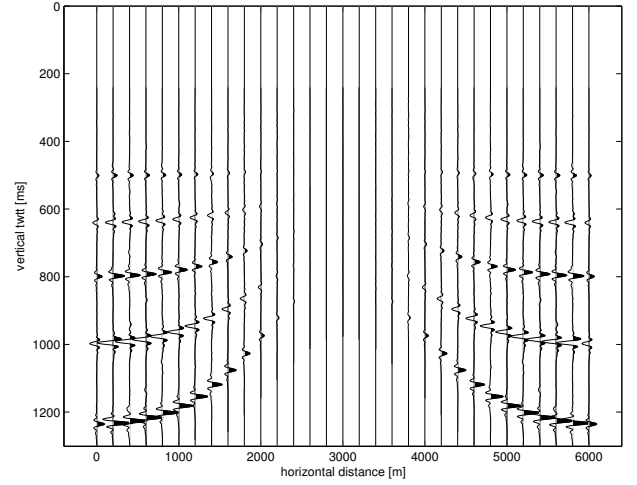

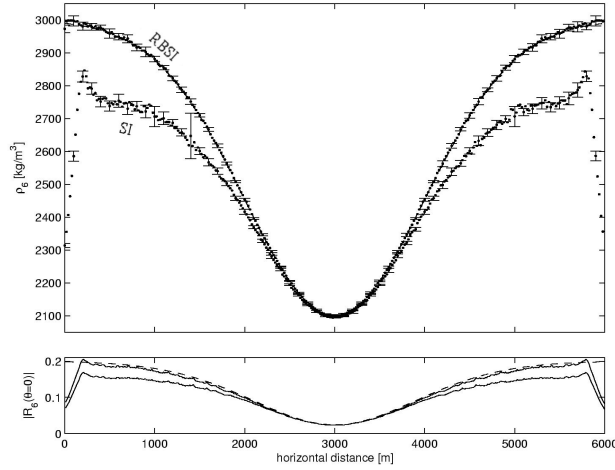Figure 6: *Difference between Fig. 5 and migration using exact density model from RBSI.*

Figure 7: *Bottom: Amplitude of lowest contrast after migration using constant-density layers (lower line) and exact density model (upper line) as compared to $R^+(\vec{x}_R, \theta_6^+ = 0)$ (dashed). Top: ρ_6 from SI and RBSI, the latter converging to desired value.*
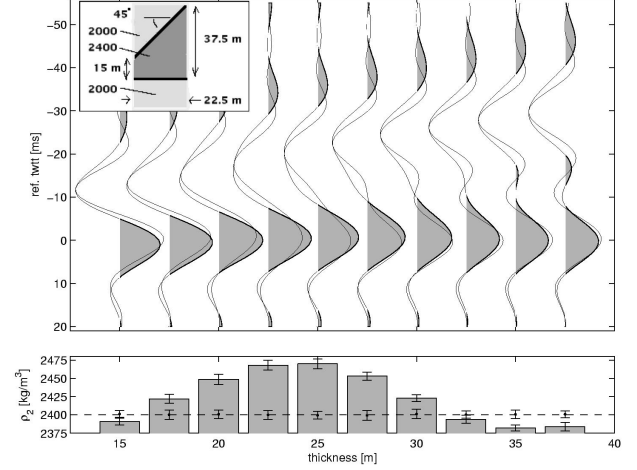

Figure 8: *Detrimental effect of wavelet stretch in wedge model using SI for density determination of middle layer. Error bars around dashed line: correct RBSI result.*
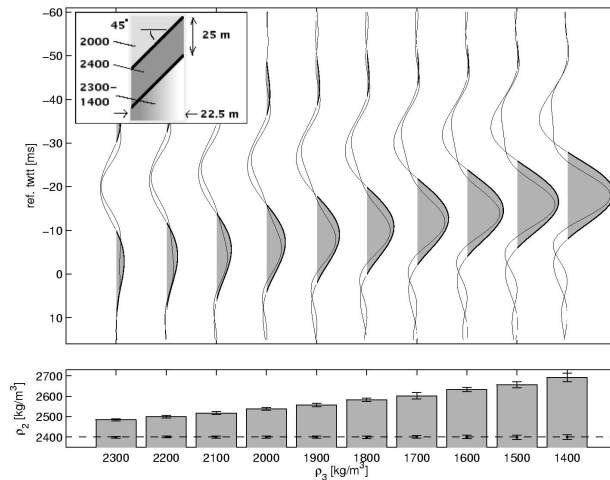

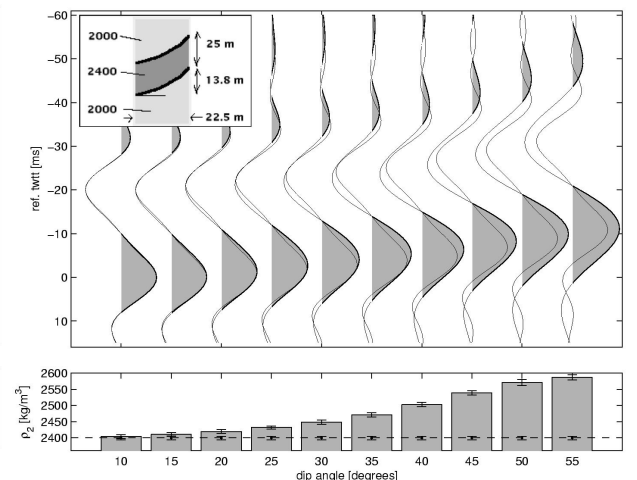Figure 9: *As in Fig. 8 but with variable reflection amplitude.*

Figure 10: *As in Fig. 8 but with variable amount of wavelet stretch.*